The Astrophysical Journal Letters, 897:L22 (8pp), 2020 July 10 https://doi.org/10.3847/2041-8213/ab9d86

Twin Jets and Close Binary Formation

Yu Saiki and Masahiro N. Machida
Department of Earth and Planetary Sciences, Faculty of Sciences, Kyushu University, Fukuoka 819-0395, Japan; machida.masahiro.018@m.kyushu-u.ac.jp
Received 2020 May 8; revised 2020 June 10; accepted 2020 June 16; published 2020 July 8

Abstract

The formation of a close binary system is investigated using a three-dimensional resistive magnetohydrodynamic simulation. Starting from a prestellar cloud, the cloud evolution is calculated until ∼400 yr after protostar formation. Fragmentation occurs in the gravitationally collapsing cloud, and two fragments evolve into protostars. The protostars orbit each other and a protobinary system appears. A wide-angle low-velocity outflow emerges from the circumbinary streams that enclose two protostars, while each protostar episodically drives high-velocity jets. Thus, the two high-velocity jets are surrounded by the low-velocity circumbinary outflow. The speed of the jets exceeds $\gtrsim$100 km s^{-1}. Although the jets have a collimated structure, they are swung back on the small scale and are tangled at the large scale due to the binary orbital motion. A circumstellar disk also appears around each protostar. In the early main accretion phase, the binary orbit is complicated, while the binary separation is within $<$30 au. For the first time, all the characteristics of protobinary systems recently observed with large telescopes are reproduced in a numerical simulation.

Unified Astronomy Thesaurus concepts: Multiple star evolution (2153); Star formation (1569); Jets (870); Magnetic fields (994); Stellar jets (1607)

Supporting material: animations

1. Introduction

A large fraction of main-sequence stars are members of binary systems, and more than half of the stars exceeding 1 $M_\odot$ are binaries (Duquennoy & Mayor 1991; Moe & Di Stefano 2017). The binary fraction of very young stars in star-forming regions is higher than that of field stars, which indicates that many stars are born as binaries (Chen et al. 2013; Duchêne & Kraus 2013). Therefore, studies into star formation should consider binary formation and not focus only on single star formation, in order to comprehensively understand the star formation process. The formation of close binaries with a separation of $\lesssim$10 au is especially important for clarifying the origin of gravitational waves, Type Ia supernovae, X-ray binaries, and carbon-enhanced metal-poor stars (Riess et al. 1998; Remillard & McClintock 2006; Abbott et al. 2016; Hansen et al. 2016). However, no convincing scenario has yet been proposed for close binary formation (Bodenheimer 2011). Past theoretical studies have proposed binary formation scenarios such as disk fragmentation, fission, and capture (Tohline 2002),[1] while observations have provided useful clues for understanding binary formation. Recent observations have unveiled newborn binary systems, where observed circumbinary disks, circumbinary outflows, and protostellar jets provide clear evidence of mass accretion occurring in the forming binary systems (Itoh et al. 2000; Itoh 2001; Hioki et al. 2007; Mayama et al. 2010; Takakuwa et al. 2012; Dutrey et al. 2014; Pyo et al. 2014; Tobin et al. 2016, 2019; Maureira et al. 2020). It is well known that protostellar jets and outflow are driven by magnetic effects in collapsing clouds (Tomisaka 2002). Recent theoretical studies have shown that the angular momentum in a gravitationally collapsing cloud is effectively transported by magnetic effects such as protostellar jets and magnetic braking (e.g., Vaytet et al. 2018). It is expected that binary formation is closely related to the mechanisms of angular momentum transport (Machida et al. 2008). Thus, we need to carefully consider the effects of the magnetic field when investigating binary systems formed in gravitationally collapsing clouds. Note that the density perturbation of the initial cloud also affects the (close) binary formation (Machida et al. 2004, 2005a; Price & Bate 2007).

Unlike the single-star formation process, binary formation is very complicated. As a result, binary formation and the fragmentation process has been investigated in three-dimensional simulations (Tsuribe & Inutsuka 1999; Matsumoto & Hanawa 2003; Goodwin et al. 2007; Hennebelle & Teyssier 2008). However, only the gas collapse phase before protostar or protobinary formation has been intensively investigated in these studies. Also, some studies have ignored the magnetic field, even though the magnetic field significantly affects both the fragmentation process and binary orbital evolution (Matsumoto et al. 2015). Circumbinary outflow and protostellar jets, which are proof of mass accretion onto a binary system, cannot be reproduced without considering the magnetic effects. Machida et al. (2009) and Kuruwita et al. (2017) investigated the formation and evolution of a binary system in three-dimensional magnetohydrodynamic (MHD) simulations and reproduced the circumbinary disk and low-velocity outflow (see also Kuruwita & Federrath 2019). However, they could not reproduce the high-velocity jets, because the protostars were not resolved in their studies. High-velocity jets driven by each protostar in a binary system have not yet been reproduced in theoretical studies, while observations are revealing high-velocity jets in binary systems (Tobin et al. 2019; Hara et al. 2020). In addition, it is not possible to investigate close binary systems without sufficient spatial resolution in numerical simulations. Using non-ideal MHD simulations, Wurster et al. (2017) investigated the formation of binary systems that show neither outflows nor jets, which is attributed to the initial

[1] Here, we commented on the formation of general binary systems but do not focus only on close binary systems.

condition adopted in their study (for details, see Section 5.5 of Wurster & Bate 2019).

2. Numerical Settings and Model

The numerical settings adopted in this study are almost the same as in Machida (2014) and Machida & Basu (2019), in which jet driving and disk formation around a single protostar were investigated. We calculate the cloud evolution from the prestellar stage until ∼400 yr after protostar (or protobinary) formation using our resistive MHD nested grid code, in which Equations (1)–(7) of Machida & Matsumoto (2012) are solved. An ohmic dissipation term is included in the induction equation, and the coefficient of ohmic resistivity is described in Machida et al. (2007). As described in Machida & Basu (2019), we adopt the stiff equation of state (EOS) method, which mimics a protostar in a high-density region without sink cells (Tomisaka 2002; Hennebelle & Ciardi 2009; Joos et al. 2012; Hirano & Bromm 2017). The equation of state used in the range of $n < 5 \times 10^{16}\,\mathrm{cm^{-3}}$ is the same as in Machida (2014), while the EOS at high densities of $n > 5 \times 10^{16}\,\mathrm{cm^{-3}}$ has a polytropic index $\gamma = 2.0$. This slight change in the EOS can accelerate the calculation, while slightly expanding the protostar (Machida & Nakamura 2015). It should be noted that we cannot use sink cells having an accretion radius $\gtrsim$1 au when investigating high-velocity jets, because the jet-driving region is embedded in the sink.

As an initial state, we take a Bonnor–Ebert (BE) sphere with a central density $n_0 = 3 \times 10^6\,\mathrm{cm^{-3}}$ and an isothermal temperature $T_{\mathrm{iso},0} = 10$ K. The radius of the initial cloud is twice the critical BE radius, which corresponds to $R_{\mathrm{cl}} = 5.3 \times 10^3$ au. To promote contraction and realize a gravitationally unstable state, the density of the BE sphere is enhanced by a factor of $f = 6.98$ where f is the density enhancement factor (for details, see Matsushita et al. 2017). Thus, the central density of the initial cloud is $n_{\mathrm{c},0} = 2.1 \times 10^7\,\mathrm{cm^{-3}}$ ($=f \times n_0$). In addition, we added 10% of the $m = 2$ mode of the density perturbation (see Machida et al. 2005b). The mass of the initial cloud is $M_{\mathrm{cl}} = 3.7\,M_\odot$. A uniform density of $2.3 \times 10^5\,\mathrm{cm^{-3}}$ is set outside the prestellar cloud. A uniform magnetic field $B_0 = 1.2 \times 10^{-4}$ G and a rigid rotation $\Omega_0 = 9.5 \times 10^{-13}\,\mathrm{s^{-1}}$ are adopted, in which the magnetic vectors are parallel to the rotation axis or the z-axis. The ratio of thermal α_0, rotational β_0 and magnetic γ_0 energy to the gravitational energy of the prestellar cloud are $\alpha_0 = 0.1$, $\beta_0 = 0.05$, and $\gamma_0 = 0.03$, respectively. The mass-to-flux ratio normalized by the critical value $(2\pi G^{1/2})^{-1}$ is $\mu_0 = 5$.

To calculate the cloud evolution and binary formation, we use the nested grid code (Machida et al. 2004). Grids having different cell widths are nested and the grid level is described by l. Each grid is composed of $(i, j, k) = (128, 128, 128)$ cells, and the grid size $L(l)$ and cell width $h(l)$ halve with each increment of the grid level. Before the calculation starts, six levels of grid $l = 6$ are set for the initial state. The initial cloud is immersed in the fourth level of the grid ($l = 5$), which has twice the cloud radius $L(5) = 1.06 \times 10^4$ au and a cell width of $h(5) = 82.6$ au. The coarsest grid has a grid size of $L(1) = 1.69 \times 10^5$ au and a cell width of $h(1) = 1332$ au. After the calculation starts, a new finer grid is generated to ensure the Truelove condition, in which the Jeans wavelength is resolved for at least 16 cells. The maximum grid level is set to $l = 16$ and has $L(16) = 5.01$ au and $h(16) = 0.039$ au.

3. Results

Figure 1 shows the time sequence of a protobinary system for ∼400 yr. Note that the structures seen in Figure 1 are very similar to those seen in Wurster et al. (2017), in which sink particles were used. This indicates that the fragmentation and binary formation process can be accurately calculated with sink particles. In the collapsing cloud, a bar-like structure develops and fragmentation occurs, as shown in Figure 1(a). The high-density region continues to collapse and a protostar forms in each fragment. Each protostar has a central density of $>10^{15}$–$10^{18}\,\mathrm{cm^{-3}}$ and a radius of $\lesssim$0.05 au. The cavity-like structures or low-density regions in the proximity of the protostars seen in Figure 1(b) are caused by magnetic interchange instability, which is usually confirmed in single-star formation simulations (e.g., Machida & Basu 2020). When fragmentation occurs, the separation between fragments or protostars is about 20 au (Figures 1(a) and (b)). As seen in Figures 1(a)–(c), the binary separation gradually shrinks during $t_{\mathrm{ps}} \lesssim 200$ yr, where t_{ps} is the elapsed time after protostar formation. The protobinary system has a minimum separation $r_{\mathrm{sep}} \sim 1$ au at $t_{\mathrm{ps}} \sim 170$ yr (Figure 1(c)). The separation then increases and maintains $r_{\mathrm{sep}} \sim$ 5–15 au by the end of the simulation (Figures 1(e) and (f)). In Figures 1(d)–(f), we can confirm that each protostar is surrounded by a circumstellar disk with a size of ∼3–5 au. In addition, a circumbinary streams encloses the two protostars and their disks with a size of 10–20 au.[2] It should be noted that the binary orbital motion would be related to the amplification of the magnetic field that may depend on the spatial resolution. Thus, we need to investigate the spatial resolution necessary to more precisely calculate the binary orbital motion in future studies.

Figures 2(a) and (b) show the density distribution at the same epoch as in Figure 1(f). At this epoch, the protostars are located along the $y = 0$ axis as shown in Figure 1(f). As seen in Figure 2(a), both protostars drive the high-velocity jets (see the animation associated with Figure 2). In addition, we can confirm cavity-likes structure above and below each protostar. On a large scale (Figure 2(b)), we cannot distinguish each jet because the protostellar jets are highly tangled. In addition to the high-velocity jets, a wide-angle low-velocity outflow is driven by the circumbinary region as shown in Figure 2(b). Note that a low-velocity outflow also appears in the outer region of each circumstellar disk. Thus, the outflow at the large scale has an internal structure that is attributed to both the tangled high-velocity jets and low-velocity outflows. The disk-like structure can be confirmed along the $z = 0$ axis in Figure 2(b). In addition, outside the protostars, we can confirm the high-density region corresponding to the circumbinary streams with a radius of ∼10–15 au in Figures 1(d)–(f). Figure 2(c) shows the ratio of azimuthal to Keplerian velocity ($v_\phi / v_{\mathrm{kep}}$), in which the central mass M_{c} is derived by the sum of the gas in the region with $n > 10^{13}\,\mathrm{cm^{-3}}$ in the range of <10 au to estimate the Keplerian velocity $v_{\mathrm{kep}} = (GM_{\mathrm{c}}/r)$. Note that the mass within the circumbinary streams are concentrated within <10 au (Figures 1(d)–(f)). The figure indicates that the rotation velocity is comparable to the Keplerian velocity in a large part of the circumbinary streams. Thus, it is natural that the circumbinary streams can drive the (low-velocity) outflow as seen in Machida et al. (2009) and

[2] Here, we call the high-density region that surrounds two protostars the circumbinary streams (red ring-like structure in Figures 1(d)–(f)).

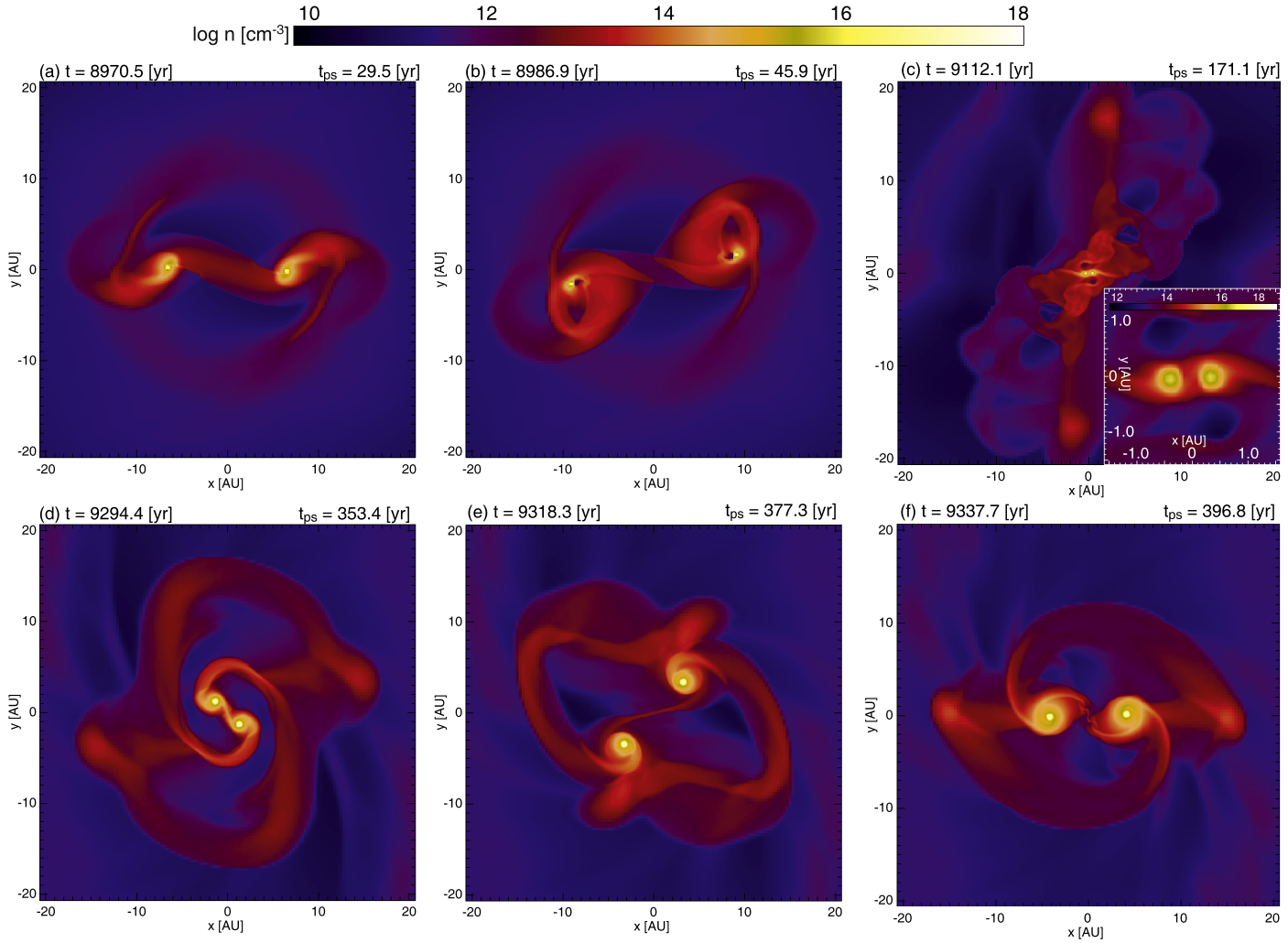

Figure 1. Density distribution (color) on the equatorial plane is plotted. The elapsed time after the cloud begins to collapse t and that after protostar formation t_{ps} are given in the upper part of each panel. The inset in panel (c) is the close-up view of the central region.

Kuruwita et al. (2017). The outgoing flow reaches ∼200 au from the protostars by the end of the simulation.

Figure 2(d) plots the outflowing mass ΔM_{out} in different outflow velocity bins ($\Delta v_r = 4\,\mathrm{km\,s^{-1}}$) at $t_{ps} = 396.8$ yr and shows that the protobinary system drives the outflow mainly in the range of $\lesssim$100 km s^{-1} at this epoch, in which a small fraction of outgoing flow exceeds 100 km s^{-1}. The figure also indicates that the low-velocity component dominates the high-velocity component. The low-velocity component is mainly driven by the circumbinary region, while the high-velocity component appears near the protostars. The local maximum around $v_r \sim 70\,\mathrm{km\,s^{-1}}$ corresponds to the high-velocity jets directly driven by each protostar.

Figure 3 shows the three-dimensional structures of the high-velocity jets at $t_{ps} = 396.8$ yr, in which the jet structures with different velocity components are delineated. At this epoch, a very small amount of the high-velocity components (>90 km s^{-1}) appears above and below the protostars and the jets are considerably distorted (Figure 3(a)), while the velocity components of 70 km s^{-1} are directly connected to the protostars (Figure 3(b)). The jet velocity of $v_{jet} \simeq 70\,\mathrm{km\,s^{-1}}$ roughly corresponds to the Keplerian velocity just outside the protostar where the Keplerian velocity $(GM_{ps}/r_{ps})^{1/2}$ becomes 57–67 km s^{-1} with a protostellar mass of $M_{ps} \simeq 0.15\,M_\odot$ (see below) and a protostellar radius of $r_{ps} \simeq 0.03$–0.04 au (Figure 2(c)). Note that a small fraction of the jet driven by each circumstellar disk and protostar can be further accelerated near the driving region (e.g., Kudoh et al. 1998) and produce the very high-velocity components (>70 km s^{-1}). The jets with $\gtrsim$50 km s^{-1} have a well-collimated structure (Figures 3(b) and (c)), while the collimation of relatively low-velocity components of $\lesssim$20 km s^{-1} is not very good. The jets are tangling on a scale of ∼40 au (Figure 3(e)), while the highly tangled jets are confirmed like a single distorted jet on a large scale (Figure 3(f)). Note that, in Figure 3(f), the cone-line structure enclosing the central jet corresponds to the outflow driven from the circumbinary region. The figure indicates that the spatial resolution of $\lesssim$100 au is required to resolve each jet driven by each protostar of close binary system in observation.

Figure 4 shows the three-dimensional structure of a protobinary system at the same epoch as in Figure 3. We can clearly confirm twin jets driven by protostars (see the animation associated with Figure 4). Because each protostar orbits in a counterclockwise fashion, the protostellar jets are somewhat swung back in the same direction. Within the jets, magnetic field lines are strongly twisted. Near the roots of the jets, the protostars are enclosed by the circumstellar disks, which are surrounded by the circumbinary streams (see also Figures 1 and 2).

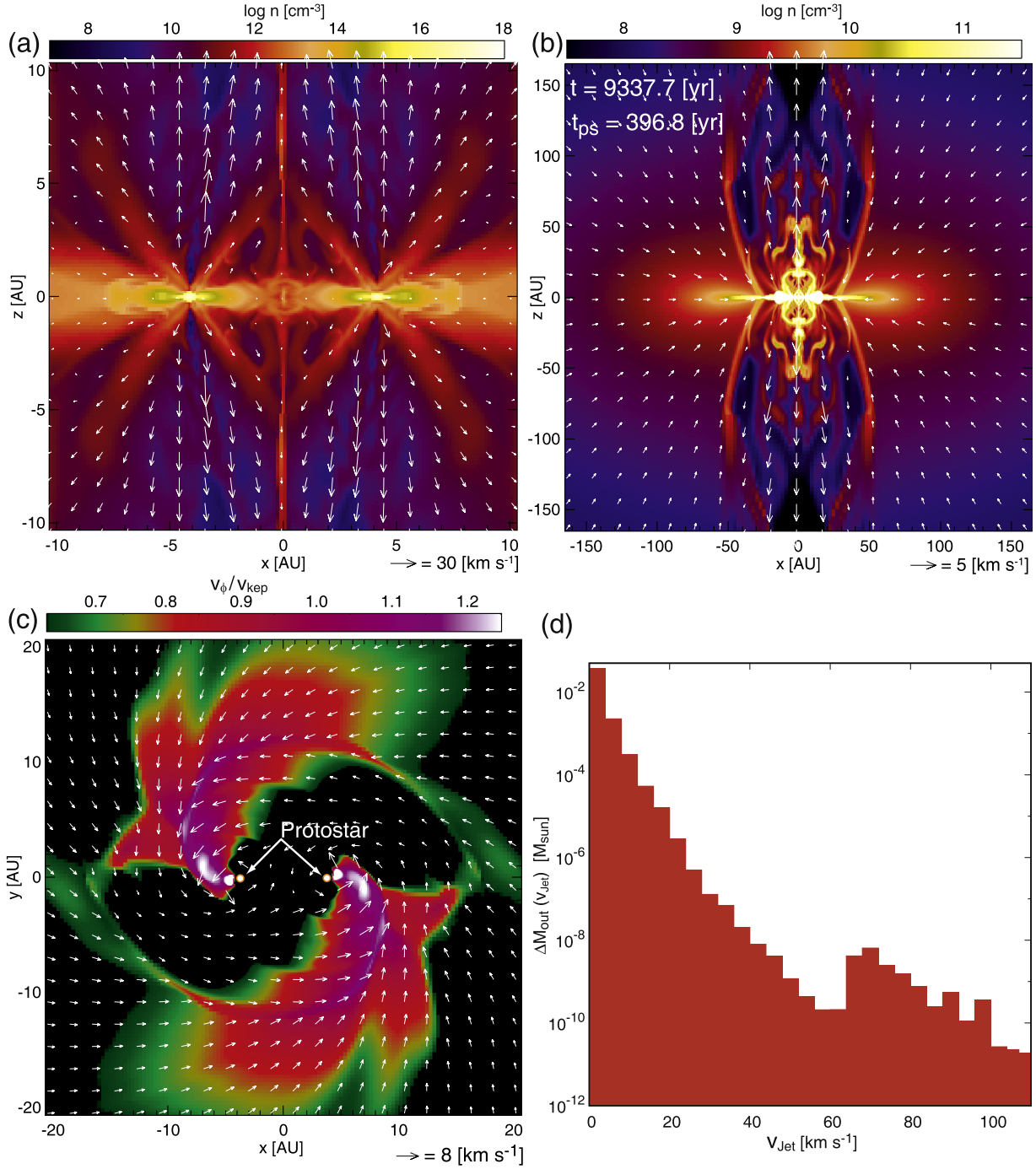

Figure 2. (a), (b) Density (color) and velocity (arrows) distributions on the $y = 0$ plane. Panel (a) is an enlarged view of panel (b). (c) Ratio of azimuthal to Keplerian velocity $v_\phi/v_{\rm kep}$ (color) and velocity distribution (arrows) on the equatorial plane. The position of protostars are indicated. (d) Histogram of outflowing gas against the outflow velocity. The elapsed time after the cloud begins to collapse, t, and that after protostar formation, $t_{\rm ps}$, are given in panel (b). The animation includes the $x = 0$, $y = 0$, and $z = 0$ planes out to ∼40 au, and a wider view of the $y = 0$ plane to ∼300 au. The animation proceeds from collapse $t = 8970$ to 9355 yr, or from $t_{\rm ps} = 29$ to 414 yr.

(An animation of this figure is available.)

The top panel of Figure 5 shows the mass of the high-density regions and outflow. Roughly, we estimated the mass of the high-density region with $n > 10^{15}\,{\rm cm}^{-3}$ as being the protostar and that with $10^{12}\,{\rm cm}^{-3} < n < 10^{15}\,{\rm cm}^{-3}$ to be the circumstellar disk, which are shown in the top panel of Figure 5. This figure indicates that the high-density region ($n > 10^{15}\,{\rm cm}^{-3}$) appears at $t = 8941$ yr, which corresponds to the protostar formation epoch ($t_{\rm ps} = 0$). Note that a temporal decrease of the mass of the high-density region ($n > 10^{15}\,{\rm cm}^{-3}$) is due to the oscillation of the high-density objects (i.e., protostars). The protostar bounces and its (average) density slightly decreases after the protostar shrinks with a temporal high mass accretion rate. The mass with $n > 10^{15}\,{\rm cm}^{-3}$ (total mass of protostars) reaches $\simeq 0.3\,M_\odot$ at the end of the simulation, while that with

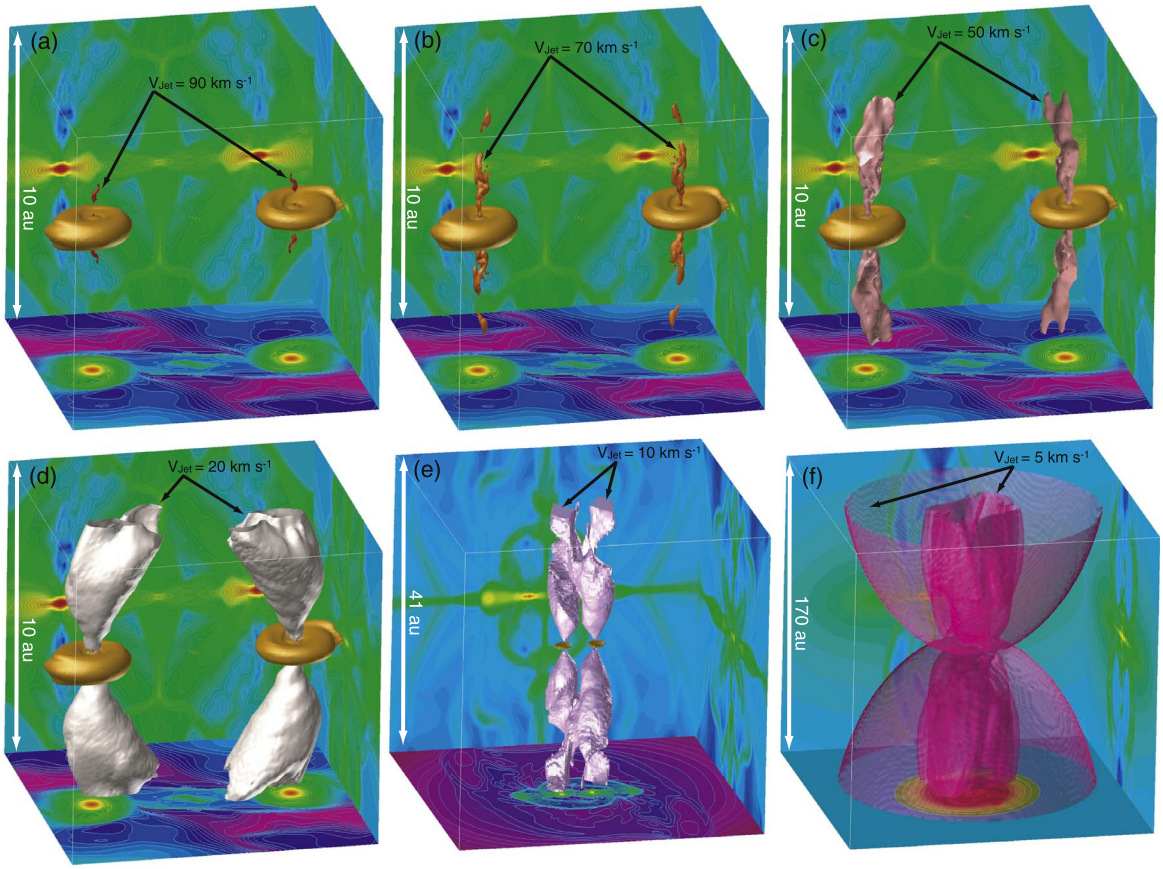

Figure 3. Structure of high-velocity jets at the same epoch as in Figure 2 with an isovelocity surface of (a) $v_{\rm Jet} = 90\,{\rm km\,s^{-1}}$, (b) $70\,{\rm km\,s^{-1}}$, (c) $50\,{\rm km\,s^{-1}}$, (d) $20\,{\rm km\,s^{-1}}$ (e) $10\,{\rm km\,s^{-1}}$ and (f) $5\,{\rm km\,s^{-1}}$. The yellow surface corresponds to the circumstellar disk with an isodensity surface of $n = 10^{13}\,{\rm cm^{-3}}$ within which a protostar is embedded. The density distribution on the $x = 0$, $y = 0$ and $z = 0$ cutting planet are projected on each wall surface. The box scale is described in each panel.

$10^{12}\,{\rm cm^{-3}} < n < 10^{15}\,{\rm cm^{-3}}$ (total mass of circumstellar disks) is $\sim 0.03\,M_\odot$ during the simulation. As there are two protostars and circumstellar disks, the mass of the protostar and circumstellar disk are estimated to be $M_{\rm ps} \simeq 0.15\,M_\odot$ and $M_{\rm disk} \simeq 0.015\,M_\odot$, respectively. On the other hand, the outflow mass, which is defined as the total mass having $v_r > 1\,{\rm km\,s^{-1}}$, increases from $M_{\rm out} \simeq 0.01\,M_\odot$ to $0.4\,M_\odot$ during the simulation, and is comparable to the protostellar mass at the end of the simulation. Thus, a significant mass ejection is realized in the protobinary system, as seen in the single-star formation process (e.g., Machida & Basu 2019).

The binary separation is also plotted in the top panel of Figure 5. The binary separation oscillates in the range of $1\,{\rm au} \lesssim r_{\rm sep} \lesssim 30\,{\rm au}$. We can see a rough correlation between the masses of the protostar, disk, and outflow, and the binary separation. To investigate the relationship between the binary separation and the outflow driving, the outflowing mass with different velocity ranges are plotted in the bottom panel of Figure 5. The figure indicates that, during the early main accretion phase, the outflow mass of the low-velocity component ($v_r = 1$–$5\,{\rm km\,s^{-1}}$) dominates that of the high-velocity component ($v_r > 5\,{\rm km\,s^{-1}}$, see also Figure 3(d)) and the low-velocity component is not significantly affected by the binary orbital motion. In addition, the low-velocity component ($v_r < 5\,{\rm km\,s^{-1}}$) appears before protostar formation $t_{\rm ps} < 0$ (or $t < 8941$ yr), while the high-velocity component ($v_r > 5\,{\rm km\,s^{-1}}$) appears $t_{\rm ps} \gtrsim 30\,{\rm yr}$ (or $t \gtrsim 8970$ yr) after protostar formation. The low-velocity outflow is originally driven by the first core (Wurster et al. 2018), which forms before protostar formation and evolves into the circumbinary structure. On the other hand, the high-velocity components are driven near the protostar where the gravitational potential has a local minimum (Figure 3). Thus, the difference in the flow emergence epochs is due to the different formation epochs of each object. It should be noted that the low-velocity flow appears before the high-velocity flow even in the single-star formation simulations (Machida & Basu 2019). Thus, the different emergence epochs of the flows is not a unique feature for the binary or multiple star formation process but universally occurs in the star formation process. In the bottom panel of Figure 5, the time variability in the outflow mass is more significant in relatively high-velocity components ($v_r > 10$–$20\,{\rm km\,s^{-1}}$) than in relatively low-velocity components ($v_r < 10\ {\rm km\,s^{-1}}$). The outflow mass in the very high-velocity components ($v_r > 20\,{\rm km\,s^{-1}}$) especially seems to correlate with the binary orbital separation, in which a strong mass ejection occurs when the binary separation becomes large.

4. Summary and Discussion

We have reproduced a protobinary system in a core-collapse simulation and confirmed the presence of protostellar jets and circumbinary outflow, which are usually observed in very young binary systems. For the first time, we have reproduced

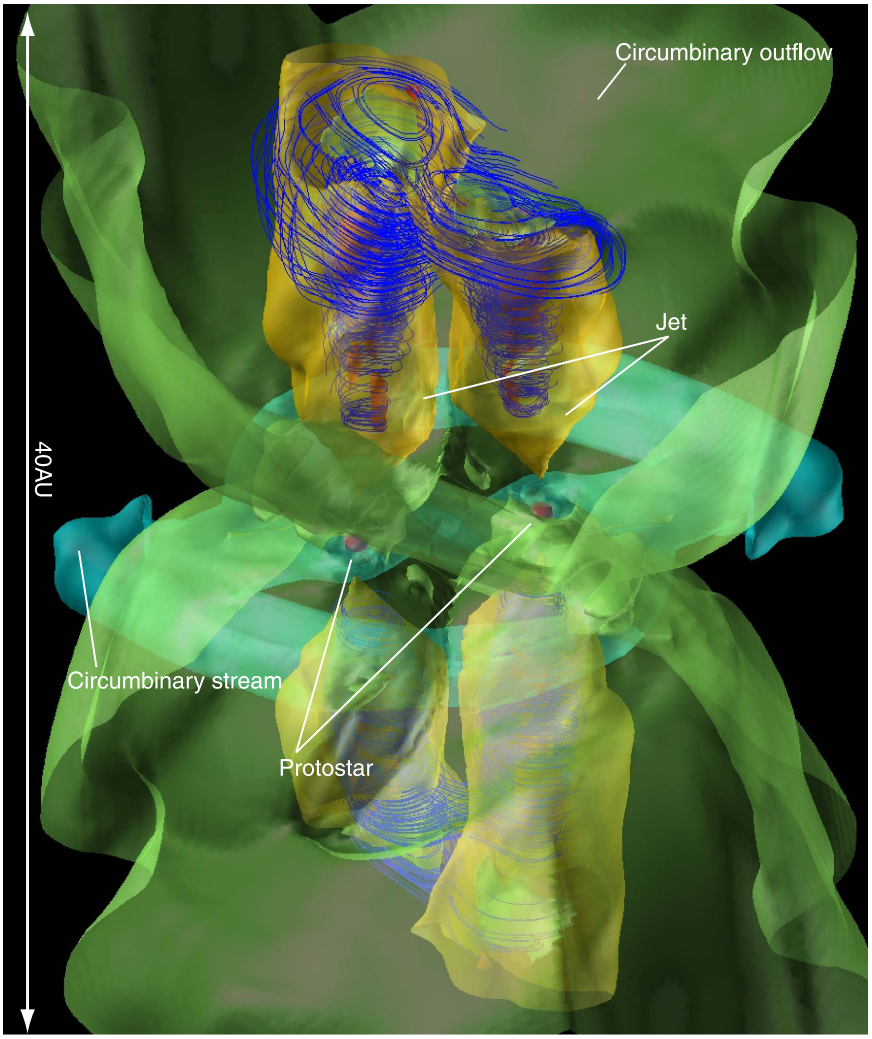

Figure 4. Three-dimensional view of protostars (red isodensity surfaces, $n = 10^{16}\,\mathrm{cm}^{-3}$), circumstellar disks, circumbinary stream (blue isodensity surfaces, $n = 10^{13}\,\mathrm{cm}^{-3}$), high-velocity jets (yellow isovelocity surfaces, $v_r = 30\,\mathrm{km\,s}^{-1}$), and circumbinary outflow (green isovelocity surfaces, $v_r = 5\,\mathrm{km\,s}^{-1}$). The blue lines are magnetic field lines. The box size is 40 au. The animation proceeds from $t_{\mathrm{ps}} = 29$–412 yr after protostar formation. The density contour on the equatorial plane is projected onto the bottom. The green surface corresponds to the isodensity surface. Other surfaces represent the jets with different velocities.

(An animation of this figure is available.)

high-velocity jets with a maximum speed of $\gtrsim 100\,\mathrm{km\,s}^{-1}$ driven by each protostar in the protobinary system, bridging the gap between theoretical studies and observations. The high-velocity components (or protostellar jets) show a significant time variability, while the low-velocity components do not show a noticeable time variability (Figure 5). In this section, we roughly estimate the necessary spatial resolution to observe the jets driven from protobinary systems. Although we conceived and referred to the simulation results, the following quantitative estimates are not directly related to quantities in the simulation. The typical timescale of the system should be determined by the binary orbital period $P = (4\pi^2 a^3/GM_{\mathrm{tot}})^{1/2}$, where a and M_{tot} are the binary orbital radius and total mass of binary protostars, respectively. Simply assuming the binary orbital radius of 10 au and total mass of $0.1\,M_\odot$, the orbital period $P = 100(a/10\,\mathrm{au})^{3/2}(M_{\mathrm{tot}}/0.1\,M_\odot)^{-1/2}$ yr is derived. We also assume that the circumbinary disk (or stream) has a radius of >10 au within which protostars are embedded. In such a case, the orbital period of the outer circumstellar disk is >100 yr. As the low-velocity outflow is driven by the circumbinary disk (or stream), which is located far from the protostars (Figure 5, bottom panel), it is not significantly disturbed by the binary orbital motion. On the other hand, the jets are easily disturbed because the jet launching points orbit with a period of <100 yr in close binary systems. Further, assuming a typical jet velocity of $30\,\mathrm{km\,s}^{-1}$, the jets reach $L_{\mathrm{Jet}} \sim 600\,(v_{\mathrm{Jet}}/30\,\mathrm{km\,s}^{-1})$ au during one orbital period of 100 yr. Note that the velocity of $30\,\mathrm{km\,s}^{-1}$ roughly corresponds to the typical jet velocity in the simulation. Thus, only jets with a size of $\ll L_{\mathrm{Jet}}$ are detectable, while a complex outflow would be detected in the range of $\gtrsim L_{\mathrm{Jet}}$. We can actually distinguish the binary jets within <100 au in the simulation (Figures 3 and 4). Resolving two protostellar jets in observations is evidence of the existence of a protobinary system. Our study showed that a close binary system with a separation of ~ 10 au can drive twin jets with a size of $\sim$10–100 au, which is observable by current telescopes.

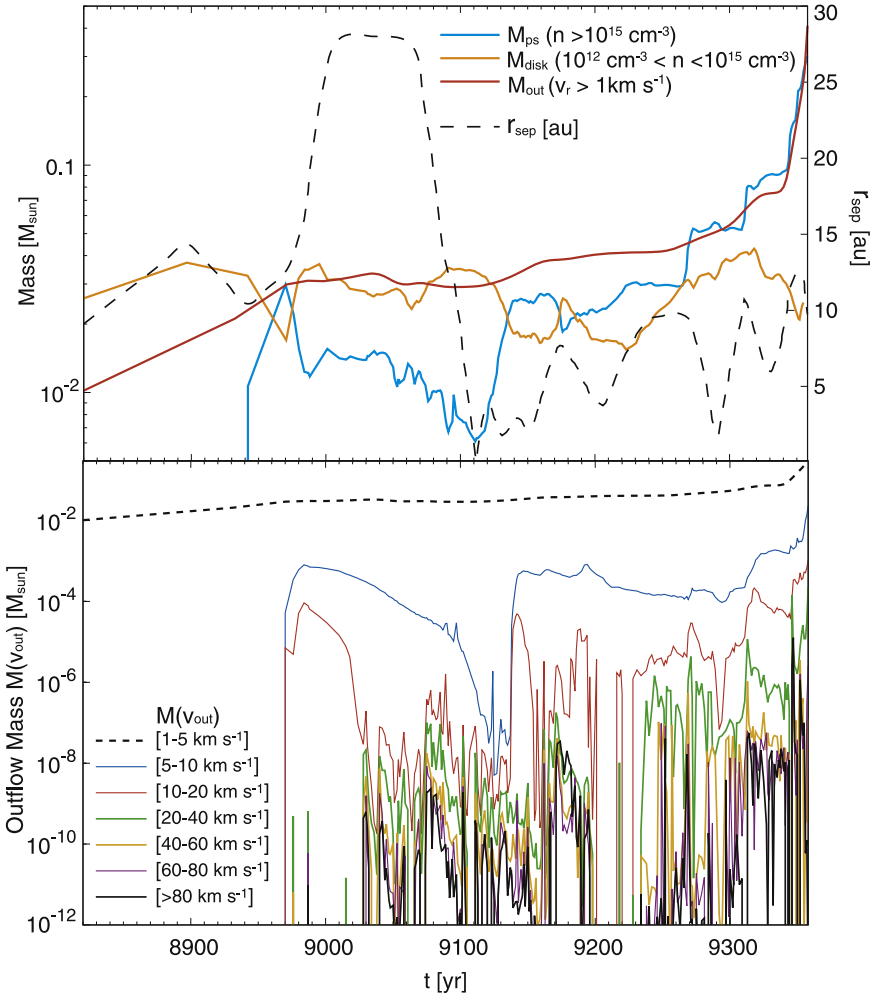

Figure 5. Protostellar, disk, and outflow mass against the elapsed time t (top; left vertical axis). Outflow mass in different velocity range against the elapsed time (bottom; left vertical axis). The binary separation r_{sep} (right axis) is plotted in the top panel.

We thank the referee for very useful comments and suggestions for this Letter. The present research used the computational resources of the HPCI system provided by the Cyber Science Center, Tohoku University and Cybermedia Center, Osaka University, Earth Simulator, JAMSTEC, through the HPCI System Research Project (Project ID: hp180001, hp190035, hp200004). The present study was supported by JSPS KAKENHI grant Nos. JP17K05387, JP17H02869, JP17H06360, and 17KK0096. The simulations reported in this Letter were also performed by 2017 and 2018 Koubo Kadai on the Earth Simulator (NEC SX-*ACE*) at JAMSTEC.

ORCID iDs

Masahiro N. Machida https://orcid.org/0000-0002-0963-0872

References

Abbott, B. P., Abbott, R., Abbott, T. D., et al. 2016, PhRvL, 116, 061102
Bodenheimer, P. H. 2011, Principles of Star Formation (Berlin: Springer)
Chen, X., Arce, H. G., Zhang, Q., et al. 2013, ApJ, 768, 110
Duchêne, G., & Kraus, A. 2013, ARA&A, 51, 269
Duquennoy, A., & Mayor, M. 1991, A&A, 500, 337
Dutrey, A., di Folco, E., Guilloteau, S., et al. 2014, Natur, 514, 600
Goodwin, S. P., Kroupa, P., Goodman, A., et al. 2007, in Protostars and Planets V, ed. B. Reipurth, D. Jewitt, & K. Keil (Tucson, AZ: Univ. Arizona Press), 133
Hansen, T. T., Andersen, J., Nordström, B., et al. 2016, A&A, 588, A3
Hara, C., et al. 2020, ApJ, submitted
Hennebelle, P., & Ciardi, A. 2009, A&A, 506, L29
Hennebelle, P., & Teyssier, R. 2008, A&A, 477, 25
Hioki, T., Itoh, Y., Oasa, Y., et al. 2007, AJ, 134, 880
Hirano, S., & Bromm, V. 2017, MNRAS, 470, 898
Itoh, Y. 2001, in IAU Symp. 200, The Formation of Binary Stars, ed. H. Zinnecker & R. D. Mathieu (Cambridge: Cambridge Univ. Press), 261
Itoh, Y., Kaifu, N., Hayashi, M., et al. 2000, PASJ, 52, 81
Joos, M., Hennebelle, P., & Ciardi, A. 2012, A&A, 543, A128
Kudoh, T., Matsumoto, R., & Shibata, K. 1998, ApJ, 508, 186
Kuruwita, R. L., & Federrath, C. 2019, MNRAS, 486, 3647
Kuruwita, R. L., Federrath, C., & Ireland, M. 2017, MNRAS, 470, 1626
Machida, M. N. 2014, ApJL, 796, L17
Machida, M. N., & Basu, S. 2019, ApJ, 876, 149
Machida, M. N., & Basu, S. 2020, MNRAS, 494, 827
Machida, M. N., Inutsuka, S.-. ichiro., & Matsumoto, T. 2007, ApJ, 670, 1198
Machida, M. N., Inutsuka, S.-. ichiro., & Matsumoto, T. 2009, ApJL, 704, L10
Machida, M. N., & Matsumoto, T. 2012, MNRAS, 421, 588
Machida, M. N., Matsumoto, T., Hanawa, T., et al. 2005a, MNRAS, 362, 382
Machida, M. N., Matsumoto, T., Tomisaka, K., et al. 2005b, MNRAS, 362, 369
Machida, M. N., & Nakamura, T. 2015, MNRAS, 448, 1405
Machida, M. N., Tomisaka, K., & Matsumoto, T. 2004, MNRAS, 348, L1
Machida, M. N., Tomisaka, K., Matsumoto, T., et al. 2008, ApJ, 677, 327
Matsumoto, T., & Hanawa, T. 2003, ApJ, 595, 913
Matsumoto, T., Onishi, T., Tokuda, K., et al. 2015, MNRAS, 449, L123
Matsushita, Y., Machida, M. N., Sakurai, Y., et al. 2017, MNRAS, 470, 1026

Maureira, M. J., Pineda, J. E., Segura-Cox, D. M., et al. 2020, arXiv:2005.11954
Mayama, S., Tamura, M., Hanawa, T., et al. 2010, Sci, 327, 306
Moe, M., & Di Stefano, R. 2017, ApJS, 230, 15
Price, D. J., & Bate, M. R. 2007, MNRAS, 377, 77
Pyo, T.-S., Hayashi, M., Beck, T. L., et al. 2014, ApJ, 786, 63
Remillard, R. A., & McClintock, J. E. 2006, ARA&A, 44, 49
Riess, A. G., Filippenko, A. V., Challis, P., et al. 1998, AJ, 116, 1009
Takakuwa, S., Saito, M., Lim, J., et al. 2012, ApJ, 754, 52
Tobin, J. J., Bourke, T. L., Mader, S., et al. 2019, ApJ, 870, 81
Tobin, J. J., Kratter, K. M., Persson, M. V., et al. 2016, Natur, 538, 483
Tohline, J. E. 2002, ARA&A, 40, 349
Tomisaka, K. 2002, ApJ, 575, 306
Tsuribe, T., & Inutsuka, S.-. ichiro. 1999, ApJL, 523, L155
Vaytet, N., Commerçon, B., Masson, J., et al. 2018, A&A, 615, A5
Wurster, J., & Bate, M. R. 2019, MNRAS, 486, 2587
Wurster, J., Bate, M. R., & Price, D. J. 2018, MNRAS, 475, 1859
Wurster, J., Price, D. J., & Bate, M. R. 2017, MNRAS, 466, 1788